Published as:
MONTGOMERY, Y. C., FOCKE, W. W. & KELLY, C. 2017. Measurement and Modelling of Pyrotechnic Time Delay Burning Rates: Method and Model Development. *Propellants, Explosives, Pyrotechnics,* 42**,** 1161-1167.

DOI: 10.1002/prep.201700107

Measurement and Modelling of Pyrotechnic Time Delay Burning Rates: Method and Model Development

Yolandi C. Montgomery,[a] Walter W. Focke,*[a] and Cheryl Kelly [b]

Abstract: The burning rates of a slow reacting $Mn+Sb_2O_3$ and a fast reacting $Si+Pb_3O_4$ time delay composition, filled into lead tubes, were measured with an infrared camera, with two thermocouples and in the form of a fully assembled detonator. The infrared camera method returned values that were on average about 12% lower than those recorded for the detonators. The temperature profiles measured for the slow burning elements were fully developed, whereas those obtained for the fast burning $Si+Pb_3O_4$ elements were not. A numerical model was developed to simulate the $Mn+Sb_2O_3$ system. Kinetic parameters were determined by least square fits to the recorded surface temperature profiles. The model made it possible to determine the effect of various property variations on the burning rate. The thermal conductivity of the delay composition was found to have the smallest impact and the heat of reaction the largest effect.

Keywords: Burning rate; finite element modeling; time delay

1 Introduction

Reliable predictive models for the burning rate in metal tubes could be useful for the design and optimization of pyrotechnic delay elements. Accurate measurement of burning rates is a prerequisite for validating such models. Several techniques are available; each with its own shortcomings with regard to safety, accuracy, physical alteration to- and even destruction of the sample. One method employs a timer that starts upon the firing of an igniter and stops when light emitted from the end of the element triggers a photoelectric cell [1]. It was implemented industrially for testing fully assembled detonators [2]. Later the photoelectric cell was replaced by a thermocouple [3]. Alternatively, two thermocouples can be used to provide both the start- and the end time triggers while simultaneously enabling continuous tracking of temperature profiles [4]. High speed cameras are suitable for compositions burning in open channels and in glass columns [5].

Klein *et al*. [6] used thermocouples to capture temperature profile evolution for kinetic analysis. A straightforward energy balance over the narrow reaction zone yielded a one-dimensional mathematical model for the propagation of the combustion wave at a constant rate [7]. Boddington *et al.* [4a, 4b, 8] applied such a 1-D model to simulate experimental temperature profiles in pyrotechnic columns. Their equation included a constant lateral heat transfer term. This approach was adapted [3] to extract kinetic parameters from temperature profile data. Though Zenin's model [9] disregards heat losses, it yielded almost identical reaction kinetic parameters [3]. This implies that lateral heat loss either did not significantly influence the reaction or that that the use of a constant heat loss factor was insufficient to account for it.

Infrared (IR) cameras are extensively used in many different high temperature applications [10]. The present investigation evaluated the use of an IR camera as an alternative method to measure the burning rate and temperature profiles in pyrotechnic delay elements. The measured temperature profiles were used to validate a three-dimensional finite element model for an entire delay element structure.

2 Experimental Section

2.1 Powder Characteristics

The $Si+Pb_3O_4$ and the $Mn+Sb_2O_3$ systems were considered with the fuel content set at 36 wt-%.

The particle sizes and BET surface areas of the reagent powders, listed in Table 1, were determined with a Mastersizer Hydrosizer 2000 and a Micromeritics TriStar II instrument respectively. Powder morphology was studied with a Zeiss Ultra 55 FESEM field emission scanning electron microscope (FESEM), fitted with an InLens detector, at an acceleration voltage of either 1 kV or 2 kV. Figure 1 shows representative images of the powder particles.

X-ray diffraction (XRD) analysis was performed on a Siemens D-501 automated diffractometer using CuKα radiation (λ = 1.5406 Å) operated at 40 kV and 40 mA. It was equipped with a divergence slit of 1° and a receiving slit of 0.05°. Samples were scanned at room temperature using a counting time of 1.5 s. All components were found to be X-ray pure. See Supplementary Information Figure S.1.

[a] *Y.C. Montgomery, W. W. Focke*
Department of Chemical Engineering,
Institute of Applied Materials, University of Pretoria,
Pretoria, South Africa
**e-mail: walter.focke@up.ac.za*
[b] *C. Kelly*
Research and Technology, AEL Mining Services,
PO Modderfontein, 1645, South Africa

Table 1: Particle size and BET surface areas

Powder	d_{50} (µm)	BET area (m^2g^{-1})
Si	1.53 ± 0.02	11.08 ± 0.38
Pb_3O_4	3.22 ± 0.02	0.74 ± 0.08
Mn	11.56 ± 0.09	0.65 ± 0.01
Sb_2O_3	0.85 ± 0.13	2.07 ± 0.00

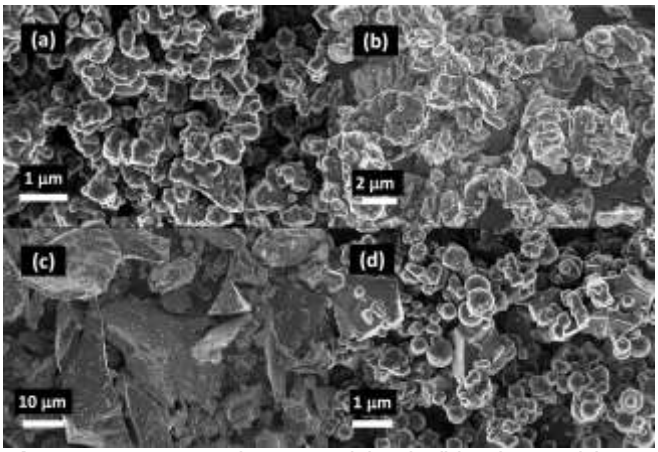

Figure 1. FESEM images. (a) Si; (b) Pb_3O_4; (c) Mn and (d) Sb_2O_3.

Thermogravimetric analysis (TGA) was performed on a Mettler Toledo A851 simultaneous TGA/SDTA instrument. About 20 mg of powder sample was placed in open 70 µL alumina pans. Temperature was scanned from 25 to 1300°C at a rate of 20°C min^{-1} with oxygen flowing at 50 mL min^{-1}. All materials showed the expected temperature dependence of the mass loss [11]. See Supplementary Information Figure S.2.

2.2 Preparation Methods

Repeated (5×) brush-mixing through a 63 µm sieve was used to break down particle agglomerates and to facilitate good mixing. The resulting binary compositions (4 g and 11 g for Si+Pb_3O_4 and Mn+Sb_2O_3 respectively) were poured into 166 mm long lead tubes with initial inner and outer diameters of 7.0 mm and 11.5 mm respectively. The ends were crimp-sealed. The tubes were then subjected to a ten-step drawing action on a proprietary rolling machine. This compressed and consolidated the powders. The final outer diameter was 6.4 mm while the length and core diameter depended on the packing density of the filled composition. The final packing density and the dimensions of the lead drawn elements tested and modelled are reported in Table 2.

2.3 Burning rate Measurements

The burning rates in the tubes were measured in three different ways. In the first method the delay elements were tested as fully assembled commercial detonators. Delay elements were prepared by cutting the rolled lead tubes into 44 mm lengths. The detonators consisted of an aluminum shell containing a section of a primary explosive (lead azide) and a high explosive (pentaerythritol tetranitrate) followed by the lead-drawn delay element. The detonators were initiated via shock tubes ignited by an electric firing device. The burning rate was determined from the time interval recorded between the triggering of a photoelectric cell and receiving a terminating signal from a pressure transducer. Tichapondwa *et al.* [12] provide a more detailed description of the test procedure.

Table 2: Geometry and packing characteristics of experimental and modelled elements

Characteristic	Si+Pb_3O_4	Mn+Sb_2O_3
D_i (mm)	2.625	2.803
D_o (mm)	6.400	6.400
$\rho_{packing}$ (kg m^{-3})	2389	4006
θ_s (-)	0.559	0.693

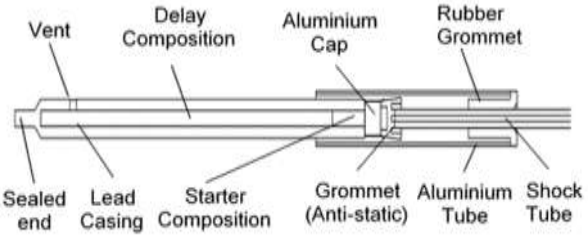

Figure 2. Delay element assembly.

The second method employed thermocouples with 100 mm lead drawn delay elements assembled as shown in Figure 2. To ensure proper contact, small holes (15 mm from each end) were drilled into the lead tubes. The thermocouples were inserted into these holes to a depth equal to the wall thickness. This was to ensure that the thermocouple did not disrupt the delay composition progression while measuring the temperature as close as possible to the combustion zone. The burning rate was determined as the time difference between specific threshold temperature rises detected by the thermocouples.

The final method employed a Dias Pyroview 380L Compact IR camera with a 50 Hz frame rate and a 384×288 pixel array. The 100 mm lead-drawn elements were positioned horizontally in front of the camera at a distance of 150 mm. The assembly, shown in Figure 2, was held with a ceramic clamp at the end of the ignition system where the rubber tube seals the shock tube. The entire delay element tube was therefore exposed to air on all sides except at the one end were the shock tube meets the starter composition. The elements were coated with a matt black high-temperature paint in order to reduce reflection and to set the emissivity as close as possible to unity.

A proprietary starter composition was used to ensure consistent ignition of the Mn+Sb_2O_3 delay compositions. A short section of the delay composition was removed from the core and replaced with a starter composition.

3 Modeling

3.1 Thermochemistry

The thermochemistry for the reaction of Mn with Sb_2O_3 was previously reported [13]. The normal redox reaction: 3Mn + Sb_2O_3 → 3MnO + 2Sb dominates in fuel-lean mixtures. In fuel-rich mixtures, an additional intermetallic reaction contributes to maintain a high exothermicity: 4Mn + Sb_2O_3 → MnSb + Sb + 3MnO. The formation of the MnSb product was confirmed through XRD analysis of the reaction products [13].

3.2 Finite Element Model

A three dimensional finite element model of the delay elements with the pyrotechnic reaction was generated. A section of the model geometry is shown in the Supplementary Information (Figure S.3). The burning delay element was modelled as a stationary tubular reactor. The reaction scheme was informed by the thermodynamic simulations reported in [13]. The reaction kinetics were modelled as a single-step autocatalytic reaction with an Arrhenius temperature dependence for the rate constant:

$$\frac{C_i}{dt} = r_i \quad (1)$$

$$r_i = k(C_B)^n (C_D)^m \quad (2)$$

$$k = k_0 \exp(-E_a/RT) \quad (3)$$

where, for the Mn+Sb_2O_3 system, C_B and C_D represent the concentrations of the oxidant and the main oxidation product (MnO) respectively.

Equation (4) constitutes an energy balance over the delay composition. The heat generated by the reaction was calculated with Equation (5). The theoretical heats of reactions were 1098 kJ mol^{-1} and 513 kJ mol^{-1} for the reactions with Si and Mn as fuels respectively.

$$\rho C_p \frac{\partial T}{\partial t} + \rho C_p u \cdot \nabla T = \nabla \cdot (\lambda \nabla T) + Q \quad (4)$$

$$Q = r_i H_{rx} \quad (5)$$

Pressed pyrotechnic compositions comprise randomly packed particles with gaps in-between. The effective thermal properties for this porous composite medium were estimated as follows [14]:

$$\lambda = \theta_s \lambda_s + (1 - \theta_s)\lambda_f \quad (6)$$

$$\rho\, Cp = \theta_s \rho_s Cp_s + (1 - \theta_s)\rho_f Cp_f \quad (7)$$

where the subscripts *s* and *f* denote the solid and fluid properties respectively. The thermal properties of the actual reagents were obtained from literature. Temperature-dependent properties were used where available. Unfortunately, the thermal conductivity of the antimony oxide powders could not be ascertained. Thermal conductivity of metal oxides usually ranges from 0.1 to 40 W $m^{-1}K^{-1}$. The lowest value was assumed for Sb_2O_3.

All phase changes occurring in the composition and in the tube wall material were taken into account. The latent heats of phase change (L) were simulated via an effective heat capacity ($C_{p,s}$) expression [15]:

$$C_{p,s}(T) = C_{p,o}(T) + L\delta(T - T_m) \quad (8)$$

where the delta function, $\delta(T - T_m)$, was approximated by a narrow Gaussian distribution centered at the corresponding transition temperatures (T_m). It applied to all melting or boiling transitions and also for the sublimation of Sb_2O_3, which occurs at 723 K [11c, 16].

Heat transfer through the element tube walls, and the surface coating, follows the solid conduction model:

$$\rho C_p \frac{\partial T}{\partial t} + \rho C_p u \cdot \nabla T = \nabla \cdot (\lambda \nabla T) + Q \quad (9)$$

Both convection and radiation heat transfer, from the paint surface to the ambient, were accounted for:

$$n \cdot (k \nabla T) = \epsilon\sigma\left(T_{amb}^4 - T^4\right) + h_{conv}(T_{ext} - T) \quad (10)$$

A temperature dependent natural convection coefficient was used [17]:

$$h_{conv} = 1.32\,[(T - T_{amb})/D_{outside}]^{0.25} \quad (11)$$

In the model, ignition was simulated by sending a temperature pulse through a copper plug located at the one end of the element. The magnitude and duration of the thermal pulse was adjusted in order to duplicate the thermal output of a 10 mm length of a Si+Pb_3O_4 starter composition.

3.3 Meshing and Solver

The finite element model was implemented using the COMSOL Multiphysics 4.3b software suite. The cylindrical symmetry of the tube meant that the 3-D elements could be modelled in 2-D. The mesh used to model the 100 mm long delay elements consisted of 38 727 triangular elements. The Newtonian solver was used to find the pseudo steady state solution at each time step. The Jacobian was calculated at every time step to ensure convergence to a tolerance of 10^{-3}. The PARDISO numerical solver was used for the transient model with row pre-ordering according to a nested dissection multi-thread algorithm.

4 Results and Discussion

4.1 Measurement techniques

Figure 3 compares burning rate measurements by the various methods for seven different compositions. It is not surprising that the burning rates measured by the various techniques were not the same. After all, in the fully assembled detonator, a sealing composition was used and the lead element was encased in an aluminum tube. However, compared to the thermocouple technique, the IR camera method returned burning rate values that were closer to those measured for the fully assembled detonators and the standard deviation was also much smaller.

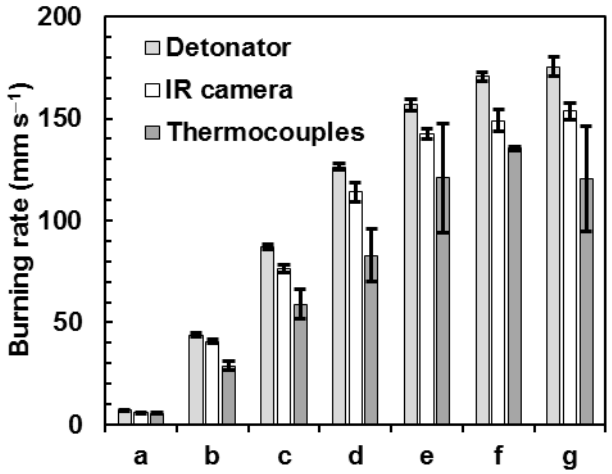

Figure 3. Burning rates measured using the three measurement techniques. (a) Mn+Sb_2O_3 at 36 wt-% fuel, and (b) to (g) Si+Pb_3O_4 containing 55, 50, 45, 40, 36 and 30 wt-% fuel respectively

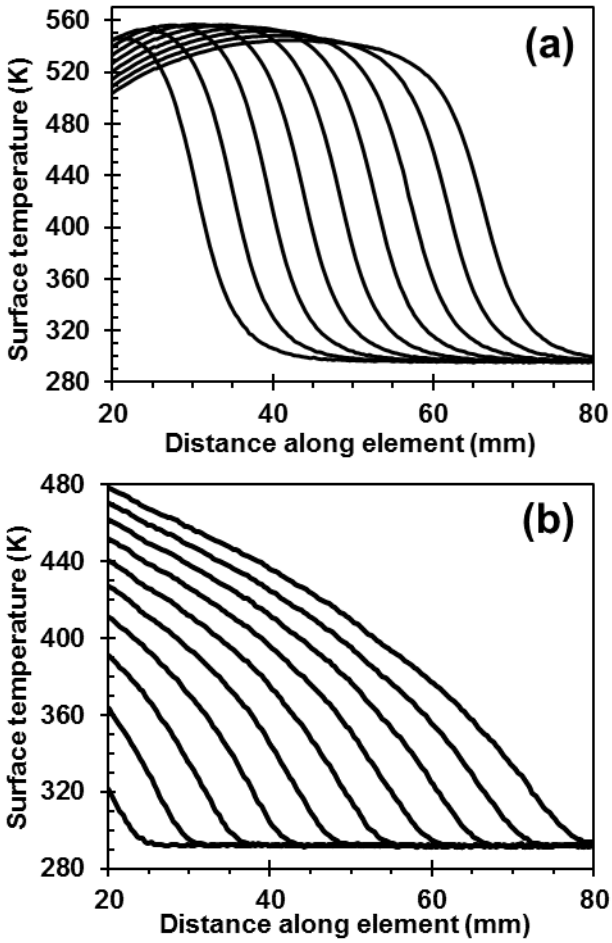

Figure 4. Temperature profiles measured using the IR camera for (a) the Mn+Sb_2O_3 reaction at time intervals of 0.8 s and (b) the Si+Pb_3O_4 at time intervals of 0.04 s.

S-type thermocouples with diameters of 1.5 mm and 3.0 mm were evaluated. The measured temperature profiles depended on the thermocouple diameter in accord with previous findings [3, 4a, 4b]. Basically, the thermocouples used in this study were too large and their response time was too slow.

Figure 4 shows temperature profiles captured with the IR camera for both the fast burning Si+Pb_3O_4 and the slow burning Mn+Sb_2O_3 systems, both at 36 wt-% fuel. The temperature profiles were fully developed for the Mn+Sb_2O_3 reaction. This facilitated direct burning rate determinations from the observed time shifts of the temperature curves. In contrast, the delay elements were too short for the Si+Pb_3O_4 reaction: the temperature profiles were still developing. In such cases a finite element model is a necessity for reliable estimation of burning rates from the temperature profile data. The procedure followed in the latter instance will be communicated separately. The present discussion is limited to the application of the finite element model to fully developed temperature profiles.

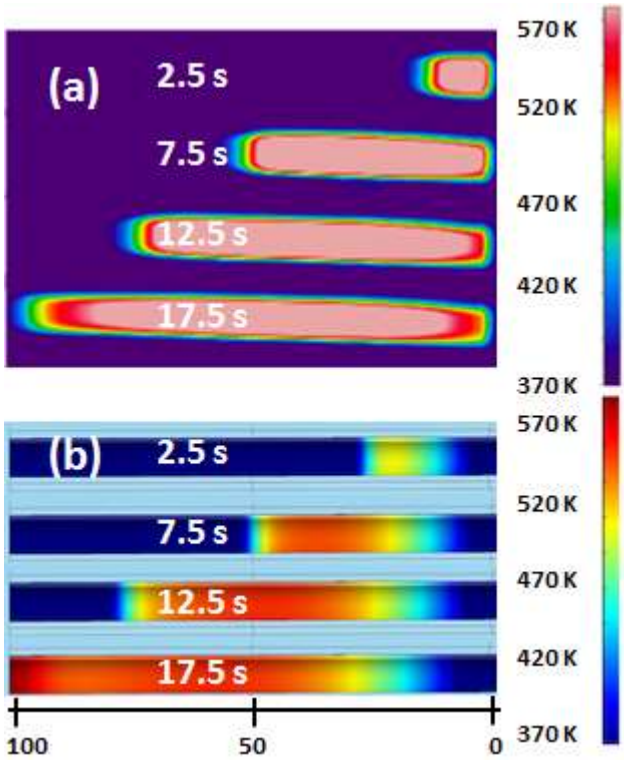

Figure 5. Progression of the Mn+Sb_2O_3 reaction wave at various times. Temperature profiles (a) captured with the IR camera, and (b) predicted by the model.

4.2 Finite Element Modelling

Figure 5 shows the progression of the reaction wave along the delay element for the Mn+Sb_2O_3 reaction as recorded by the IR camera together with the temperature distribution predicted by the finite element model on the outside surface of the element.

The kinetic parameters (n, m, E_a and k_o) were determined by comparing model predictions to IR camera-recorded temperature profiles on the outside surface of the delay element. The fitting was limited to the section 20 mm to 80 mm in order to avoid the influence of end effects. A least square data regression analysis yielded the results presented in Table 3. During the fitting process it was found that

increasing the reaction order slows the initial temperature rise. Increasing the activation energy steepened the temperature rise in the linear temperature regions. Figure 6 shows fitted temperature profiles over the length of the element.

Table 3. Finite element model best-fit kinetic parameters for the reaction of Mn with Sb_2O_3.

Parameter	n	m	E_a (kJ mol^{-1})	k_o (m^{3}mol^{-1}s^{-1})
Value	8	1	30	2.75 x10^{-28}

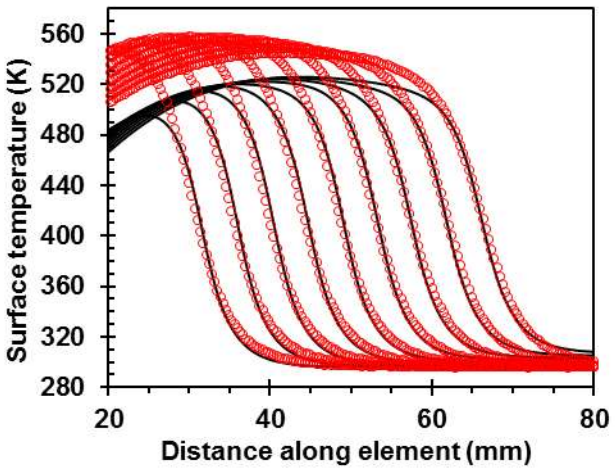

Figure 6. Surface temperature profiles in 0.8 s intervals as measured using the IR camera (O) and modelled from the best-fit kinetics (—).

Figure 6 indicates acceptable agreement between experimental results and the predictions of the model. However, the model predicted peak temperatures that were about 20 K lower than those inferred from the IR camera results. In addition, the images show a surprisingly fast cooling of the simulated lead wall which is in conflict with the IR results. Enhanced axial heat loss caused by the presence of the high thermal conductivity copper plug present in the model provides a possible explanation. The discrepancy could also be due to inaccurate estimates for the physical properties of the materials present in the delay element, in particular those for the oxides. For this reason, a sensitivity analysis was performed. Figure 7 illustrates the effect on the burning rate when the property values (λ, c_p, ρ and H_{rx}) were increased by 5, 10, 15, 20 or 40%.

Figure 7 shows that variations in the thermal conductivity had a minor impact on the model output. This vindicates the assumptions made regarding the thermal conductivity of the oxide materials. The properties c_p and ρ only enter the model as the composite variable ρc_p. When either ρ or c_p was increased by 20%, the reaction wave died before reaching the other end of the element. The same happened when the thermal conductivity was increased by 40%. The heat of reaction, H_{rx}, had the most significant effect on the burning rate.

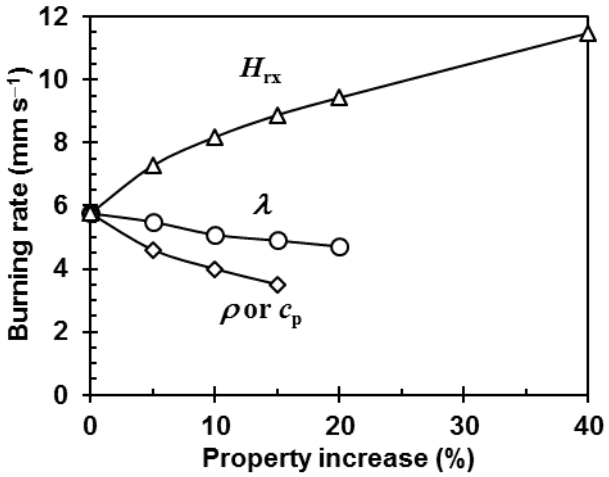

Figure 7. Sensitivity of the model to thermo-physical parameters of the delay composition.

The effect of the black paint layer on the elements was also evaluated. Figure 8 shows a cross sectional view of a section of the element during the reaction. The temperature change across the paint coating was about 25 K, so it did have a small impact on heat transfer. Figure 8 also shows the temperature distribution along the radial direction generated by the wave moving along the length of the element.

According to the model, increasing the activation energy flattened and widened the temperature profile. The reaction propagation temperature peaked around 1000 K as indicated in Figure 8. This is below the melting point of Mn but above the sublimation temperature of Sb_2O_3.

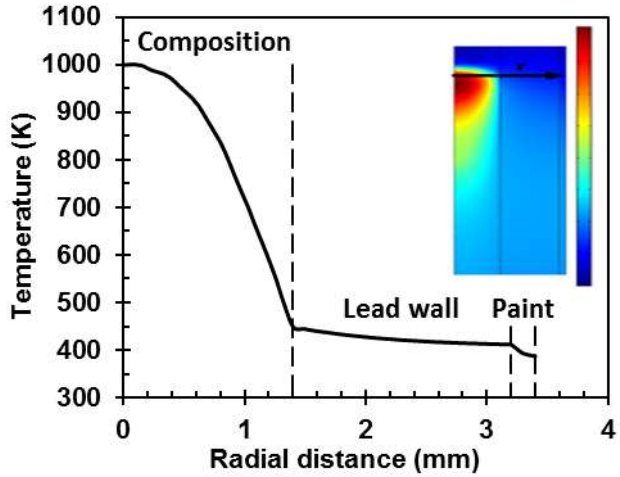

Figure 8. Temperature profile across a section of the delay element, showing the effect of the heat transfer resistance layers.

5 Conclusions

The burning rates of pyrotechnic delays in rolled lead tubes were measured using a pair of thermocouples, with an infrared (IR) camera, and destructively with the delays assembled into detonators. IR camera measurements gave slightly lower values than those measured for the detonators. The thermocouple measurement returned even lower values. It is possible that the access holes drilled into

the lead tube disturbed the temperature profiles in the burning column. The temperature rises recorded by the IR camera were steeper than those observed using the thermocouples. The measured temperature profiles, for the slow burning delay composition, were fully developed. This allowed the calibration of a numerical model that was implemented using the COMSOL Multiphysics software. The numerical model was able to reproduce the temporal evolution of the surface temperature profiles along the burning tube. However, the predicted maximum temperatures were lower than those actually measured with the IR camera. The numerical model was used to gauge the sensitivity of the predicted burning rate to variations in the thermo-physical property values. It was found that the thermal conductivity had the smallest effect while the heat of reaction had the highest impact on the predicted burning rate. The heat capacity and the density were also found to be important as upward property changes exceeding 15% led to the reaction dying out inside the metal tube.

Future studies could investigate the effects of ambient conditions, the rates of lateral heat transfer and reaction kinetics parameters on burning rates. More detailed analysis of the fast $Si+Pb_3O_4$ reaction, with its undeveloped temperature profiles, is also indicated.

The presented analysis utilized an empirical kinetic expression developed for (and hence is also limited to) a fixed stoichiometry. Proper mechanistic models, able to quantify the effects of particle size distributions, the degree of compaction, stoichiometry, etc. on reaction kinetics, are required for the development of fully predictive models.

Symbols

C	Concentration	mol m^{-3}
c_p	Heat Capacity	J $kg^{-1}K^{-1}$
D	Diameter	m
E_a	Activation energy	J mol^{-1}
H_{rx}	Molar heat of reaction	J mol^{-1} oxidant
h_{conv}	Convective heat transfer coefficient	W $m^{-2}K^{-1}$
h_t	Lateral heat transfer coefficient	W $m^{-2}K^{-1}$
k	Reaction constant	$mol^{-(n+m-1)}m^{3(n+m-1)}s^{-1}$
k_o	Arrhenius constant	$mol^{-(n+m-1)}m^{3(n+m-1)}s^{-1}$
L	Latent heat	J kg^{-1}
m, n	Reaction orders	-
Q	Heat generated	W m^{-3}
R	Universal gas constant	J $mol^{-1}K^{-1}$
r	Radius	mm
r_i	Reaction rate	mol $m^{-3}s^{-1}$
T	Temperature	K
T_{m}	Melting temperature	K
T_{ext}	External layer temperature	K
T_{amb}	Ambient temperature	K
t	Time	s
u	Linear velocity	m s^{-1}
V	Volume	m^3
v_{rx}	Average burning rate	mm s^{-1}

Greek

ε	Emissivity	-
λ	Thermal conductivity	W $m^{-1}K^{-1}$
θ_s	Volume fraction solids	-
ρ	Density	kg m^{-3}
σ	Stefan-Boltzmann constant	W $m^{-2}K^{-4}$

Acknowledgements

Financial support from AEL Mining Services and the THRIP programme of the Department of Trade and Industry and the National Research Foundation is gratefully acknowledged.

References

[1] S. S. Al-Kazraji, G. J. Rees, The fast pyrotechnic reaction of silicon and red lead: heats of reaction and rates of burning, *Fuel* **1979**, *58*, 139-143.

[2] J. T. Hedger, Factors Influencing the Pyrotechnic Reaction of Silicon and Red Lead, *Propellants, Explos., Pyrotech.* **1983**, *8*, 95-98.

[3] J. Jakubko, Combustion of the Silicon-Red Lead System. Temperature of Burning, Kinetic Analysis and Mathematical Model, *Combust. Sci. Technol.* **1999**, *146*, 37-55.

[4] [4a] T. Boddington, P. G. Laye, J. Tipping, D. Whalley, Kinetic Analysis of Temperature Profiles of Pyrotechnic Systems, *Combust. Flame* **1986**, *63*, 359-368; [4b] T. Boddington, P. G. Laye, J. R. G. Pude, J. Tipping, Temperature Profile Analysis of Pyrotechnic Systems, *Combust. Flame* **1982**, *47*, 235-254; [4c] I. M. M. Ricco, W. W. Focke, C. Conradie, Alternative oxidants for Silicon fuel in Time-Delay Compositions, *Combust. Sci. Technol.* **2004**, *176*, 1565-1575; [4d] E. L. Charsley, M. C. Ford, D. E. Tolhurst, S. Baird-Parker, T. Boddington, P.G. Laye Differential Thermal Analysis and temperature profile analysis of Pyrotechnic Delay systems: Mixtures of Tungsten and Potassium Dichromate, *Thermochim. Acta* **1978**, *25*, 131-141.

[5] E. J. Miklaszewski, A. P. Shaw, J. C. Poret, S. F. Son, L. J. Groven, Performance and aging of Mn/MnO_2 as an environmentally friendly energetic time delay composition, *ACS Sustainable Chem. Eng.* **2014**, *2*, 1312-1317.

[6] R. Klein, M. Mentser, G. von Elbe, B. Lewis, Determination of the Thermal Structure of a Combustion Wave by Fine Thermocouples, *J. Phys. Chem.* **1950**, *54*, 877-884.

[7] [7a] M. W. Beck, M. E. Brown, D. Cawthorne, Pyrotechnic delay compositions, *ChemSA* **1984**, *June*, 398-399,401; [7b] A. P. Hardt, P. V.

Phung, Propagation of Gasless Reactions in Solids-I. Analytical study of Exothermic Intermetallic Reaction Rates, *Combust. Flame* **1973**, *21*, 77-89; [7c] T. P. Ivleva, P. M. Krishenik, K. G. Shkadinskii, Nonidentity of steady conditions of combustion of gas-free mixed compositions, *Fiz. Goreniya Vzryva* **1983**, *19*, 87-90; [7d] A. G. Strunina, A. N. Firsov, S. V. Kostin, Transition modes in the combustion of heterogeneous systems with solid-phase products, *Fiz. Goreniya Vzryva* **1981**, *17*, 24-30; [7e] A. G. Strunina, T. M. Martem'yanova, V. V. Barzykin, V. I. Ermakov, Ignition of gasless systems by a combustion wave, *Fiz. Goreniya Vzryva* **1974**, *10*, 518-526; [7f] K. G. Shkadinskii, B. I. Khaikin, A. G. Merzhanov, Propagation of a pulsating exothermic reaction front in the condensed phase, *Fiz. Goreniya Vzryva* **1971**, 19-28; [7g] K. G. Shkadinskii, Transition to steady-state combustion of Gasless compositions ignited by a hot surface, *Fiz. Goreniya Vzryva* **1971**, *7*, 332-336.

[8] [8a] T. Boddington, A. Cottrell, P. G. Laye, A Numerical Model of Combustion in Gasless Pyrotechnic Systems, *Combust. Flame* **1989**, *76*, 63-69; [8b] T. Boddington, A. Cottrell, P. G. Laye, Combustion Transfer in Gasless Pyrotechnics, *Combust. Flame* **1990**, *79*, 234-241.

[9] A. A. Zenin, Thermal Structure of Solid Flames, *Pure Appl. Chem.* **1990**, *62*, 889-897.

[10] [10a] G. M. Carlomagno, G. Cardone, Infrared thermography for convective heat transfer measurements, *Exp. Fluids* **2010**, *49*, 1187-1218; [10b] S. Nagarajan, W. H. Chen, B. A. Chin, Infrared sensing for adaptive arc welding, *Weld. J. (Miami, FL, U. S.)* **1989**, *68*, 462-466.

[11] [11a] D. Swanepoel, O. Del Fabbro, W. W. Focke, Manganese as Fuel in Slow-Burning Pyrotechnic Time Delay Compositions, *Propellants, Explos., Pyrotech.* **2010**, *35*, 105-113; [11b] S. S. Al-Kazraji, G. J. Rees, The Fast Pyrotechnic Reaction of Silicon and Red Lead Part 1. Differential Thermal Analysis Studies, *Combust. Flame* **1978**, *31*, 105-113; [11c] S. E. Golunski, D. Jackson, Antimony Oxides: a Guide to Phase Changes During Catalyst Preparation, *Appl. Catal.* **1989**, *48*, 123-135.

[12] S. M. Tichapondwa, W. W. Focke, O. Del Fabbro, C. Kelly, Calcium Sulfate as a Possible Oxidant in "Green" Silicon-based Pyrotechnic Time Delay Compositions, *Propellants, Explos., Pyrotech.* **2010**, *35*, 1-9.

[13] Y. C. Montgomery, W. W. Focke, M. Atanasova, O. Del Fabbro, C. Kelly, $Mn+Sb_2O_3$ Thermite/Intermetallic Delay Compositions, *Propellants, Explos., Pyrotech.* **2016**, *41*, 919-925.

[14] A. S. Mujumdar, *Handbook of industrial drying*, 3 ed., CRC Press, New York **2006**, p. 93-95.

[15] A. P. Aldushin, V. A. Vol'pert, V. P. Filipenko, Effect of reagent melting on combustion stability for gasless systems, *Fiz. Goreniya Vzryva* **1987**, *23*, 35-41.

[16] P. W. Centers, Sublimation-controlled oxidation of antimony trioxide, *J. Solid State Chem.* **1988**, *72*, 303-308.

[17] American Society of Heating, Refrigerating and Air-Conditioning Engineers, *1997 ASHRAE handbook: Fundamentals,* ASHRAE, Atlanta **1997***,* p. 3.12.